FULL PAPER

Magnetic Resonance in Medicine

Trajectory correction based on the gradient impulse response function improves high-resolution UTE imaging of the musculoskeletal system

Sophia Kronthaler[1] 🆔 | **Jürgen Rahmer[2]** 🆔 | **Peter Börnert[2]** | **Marcus R. Makowski[1]** | **Benedikt J. Schwaiger[1]** | **Alexandra S. Gersing[1]** | **Dimitrios C. Karampinos[1]**

[1]Department of Diagnostic and Interventional Radiology, Technical University of Munich, Munich, Germany

[2]Philips Research, Hamburg, Germany

Correspondence
Sophia Kronthaler, Department of Diagnostic and Interventional Radiology, Klinikum rechts der Isar, Technische Universität München, Ismaninger Str. 22, 81675 Munich, Germany.
Email: sophia.kronthaler@tum.de

Purpose: UTE sequences typically acquire data during the ramping up of the gradient fields, which makes UTE imaging prone to eddy current and system delay effects. The purpose of this work was to use a simple gradient impulse response function (GIRF) measurement to estimate the real readout gradient waveform and to demonstrate that precise knowledge of the gradient waveform is important in the context of high-resolution UTE musculoskeletal imaging.

Methods: The GIRF was measured using the standard hardware of a 3 Tesla scanner and applied on 3D radial UTE data (TE: 0.14 ms). Experiments were performed on a phantom, in vivo on a healthy knee, and in vivo on patients with spine fractures. UTE images were reconstructed twice, first using the GIRF-corrected gradient waveforms and second using nominal-corrected waveforms, correcting for the low-pass filter characteristic of the gradient chain.

Results: Images reconstructed with the nominal-corrected gradient waveforms exhibited blurring and showed edge artifacts. The blurring and the edge artifacts were reduced when the GIRF-corrected gradient waveforms were used, as shown in single-UTE phantom scans and in vivo dual-UTE gradient-echo scans in the knee. Further, the importance of the GIRF-based correction was indicated in UTE images of the lumbar spine, where thin bone structures disappeared when the nominal correction was employed.

Conclusion: The presented GIRF-based trajectory correction method using standard scanner hardware can improve the quality of high-resolution UTE musculoskeletal imaging.

KEYWORDS
eddy currents, gradient imperfections, k-space trajectory distortions, MRI, short T_2^* species, UTE imaging

1 | INTRODUCTION

A variety of tissue components have short T_2 relaxation times.[1,2] In conventional MRI, short-T_2 tissues appear as signal voids and are not directly visible.[3] UTE imaging is an approach that allows the detection of such short-T_2 signal components. UTE sequences have received increasing interest, especially in studies of the musculoskeletal (MSK) system, thanks to their ability to visualize short-T_2 tissue components such as those within cartilage,[4] knee menisci,[5] ligaments,[6] tendons, cortical bone,[7] and other similar examples.[7-10] Many of the above MSK tissues are associated with thin structures and therefore require high-resolution imaging. For instance, cartilage in the knee measures between 2 and 7 mm thick and has been shown to include short-T_2 components with T_2 relaxation times in the order of 1 to 4 ms.[11-13] Separately, the mean thickness of cortical bone in the lumbar spine is found to be on the order of 0.3 mm, with short T_2 relaxation times of 0.1 to 1 ms.[7,14-16]

UTE imaging is usually implemented along non-Cartesian trajectories to achieve data acquisition at UTEs. Data are acquired as soon as possible after the RF excitation and during the ramping up of the readout gradient. Due to the high slew rate and the time-varying gradients, effects including system delays, eddy currents, and the filter characteristics of the entire gradient chain can significantly degrade UTE image quality.[3,17] To obtain high-quality UTE images, a precise knowledge of the dynamic gradient fields, employed to perform the non-Cartesian spatial encoding, is required. Clinical scanners use preemphasis compensation and actively shielded gradients to minimize k-space trajectory deviations. However, the gradient waveform preemphasis is typically optimized for conventional clinical acquisition needs and for scanning with Cartesian sequences. The hardware preemphasis is calibrated to meet defined filter characteristics and is limited by a finite number of time constants to correct long-term eddy currents,[18] rendering them not perfect for correcting short time-constant eddy currents.[19,20]

A number of different techniques for the characterization of non-Cartesian trajectories have been proposed, including methods that require calibration scans and measure the gradient waveforms using either special NMR field probes[21-23] or the MRI scanner hardware.[24-30] Other techniques aim to extract such supporting information for k-space trajectory correction directly from the measured raw data without any calibration scans.[31,32] Once the gradient waveform is estimated, the corrected k-space trajectories are used for image reconstruction. Different approaches have been presented specifically in the context of UTE imaging, including methods that measure the actual k-space trajectories immediately before each UTE measurement for a given set of scan parameters[33-35] or that calibrate eddy current models individually to the scan parameters to obtain an appropriate correction for arbitrary UTE scan settings.[17,36,37] Approaches that measure the actual k-space trajectories prior to each acquisition lengthen the total scan time, whereas model-based approaches necessitate a model that accurately considers not only eddy current effects but also other system delays and potentially mechanical vibrations. To better capture the different factors affecting the final actual gradient waveforms and to remove unnecessary model assumptions, it has been shown that the gradient system can be comprehensively characterized by the gradient impulse response function (GIRF).[24,38] Once the GIRF is estimated, arbitrary gradient waveforms, generated from any type of pulse sequence, can be corrected without any assumptions about the underlying mechanisms generating the gradient waveform deviations. GIRF measurements can be performed using either special NMR field probes[21-23,38] or using the thin slice method in simple phantoms.[24,30,39-41] It has been recently shown how gradient imperfections can impose spatially dependent artifacts in UTE images, which compromise the bone water quantification accuracy.[42,43] However, to the best of the author's knowledge, there has been no systematic investigation of the impact of gradient imperfection in high-resolution UTE MSK imaging.

The purpose of this work is to 1) propose a k-space trajectory correction for UTE imaging based on GIRF measurements using the thin slice method, which does not rely on additional hardware, and 2) apply the proposed correction method in high-resolution MSK UTE imaging. The proposed GIRF-based UTE trajectory correction method was first validated in a phantom and then was applied in vivo to study the influence of the trajectory correction, especially with regard to the high-frequency features in high-resolution UTE imaging of MSK tissues.

2 | METHODS

2.1 | Measurement of the GIRF

The GIRF measurement was based on a method introduced by Rahmer et al[40] and was simplified for the application in high-resolution UTE imaging. The following section summarizes key concepts of the applied GIRF measurement: A common assumption in most techniques applied in gradient chain characterization is that the MRI gradient chain can be modeled by a linear time-invariant system.[19] Such a system can be described by the impulse response function h(t), which is equivalent to the time-domain response of the system to an idealized point impulse.[44] Under the linear time-invariant system assumption, the gradient chain is thus described by the GIRF in the context of MRI. The convolution of the input gradient with the GIRF yields the real gradient as it is played out in the scanner bore.

$$g_{real}(t) = \int_{-\infty}^{+\infty} h(t-\tau) \cdot g_{input}(t). \tag{1}$$

Equation (1) can be transformed to the frequency domain, resulting in

$$G_{real}(\omega) = H(\omega) \cdot G_{input}(\omega), \tag{2}$$

where $H(\omega)$ is the gradient modulation transfer function (GMTF), which is the Fourier transform of the GIRF.[40]

To measure the behavior of the gradient system, Duyn et al[30] introduced a method based on the excitation of a thin slice yielding the generation of a virtual 1D probe without needing any additional hardware (Figure 1A). The signal obtained from this 1D test probe was then used to measure the response of a test gradient, applied along the direction of the slice selection gradient. The difference between the measured signal phase with gradients applied with positive and negative gradient polarity, respectively, yielded the linear response that is only related to the test gradient.[39] In order to account for the spatial variation of the system response, several slices at different off-center locations were excited. Rahmer et al. added a phase encoding gradient in order to measure the 3D GIRF. They showed that looking at the 3D GIRF, one finds that second order components are negligible; thus, the 3D

GIRF measurement could in principle be replaced by a 1D GIRF measurement without changing the outcome.

Therefore, in this work a simplified measurement method was applied that measures the signal from 4 slices per gradient axis to estimate the first order response. A second order polynomial was fitted per gradient axis to only improve the quality of the fit (Supporting Information Figure S3). The real gradient waveform was calculated using the first order component of the fitted phase.

The GIRF was measured in a spherical phantom (diameter 166 mm, volume 2 liters) filled with $CuSO_4$-doped water, resulting in a $T_1 \approx 280$ ms and a $T_2 \approx 240$ ms (values at 3 Tesla [T]). An excitation pulse with length 1.6 ms, maximum amplitude of 5.45 μ Tesla, and a flip angle of 45° was used to excite a 1.5 mm thick slice. To establish a high spectral density in the frequency range of interest for the GIRF measurements, a chirp waveform was played out as the input gradient with a frequency range of 0.1 to 10.0 kHz and an acquisition window of 80 ms, resulting in a frequency resolution of 12.5 Hz (Figure 1B). The acquisition window was determined based on a compromise between high-frequency resolution and adequate signal for the phantom's relaxation times. During the acquisition time, the gradient frequency increased linearly. To avoid ringing in the frequency response, the time-domain gradient waveform was ramped down by the multiplication with a half-Gaussian.[38] The measurement
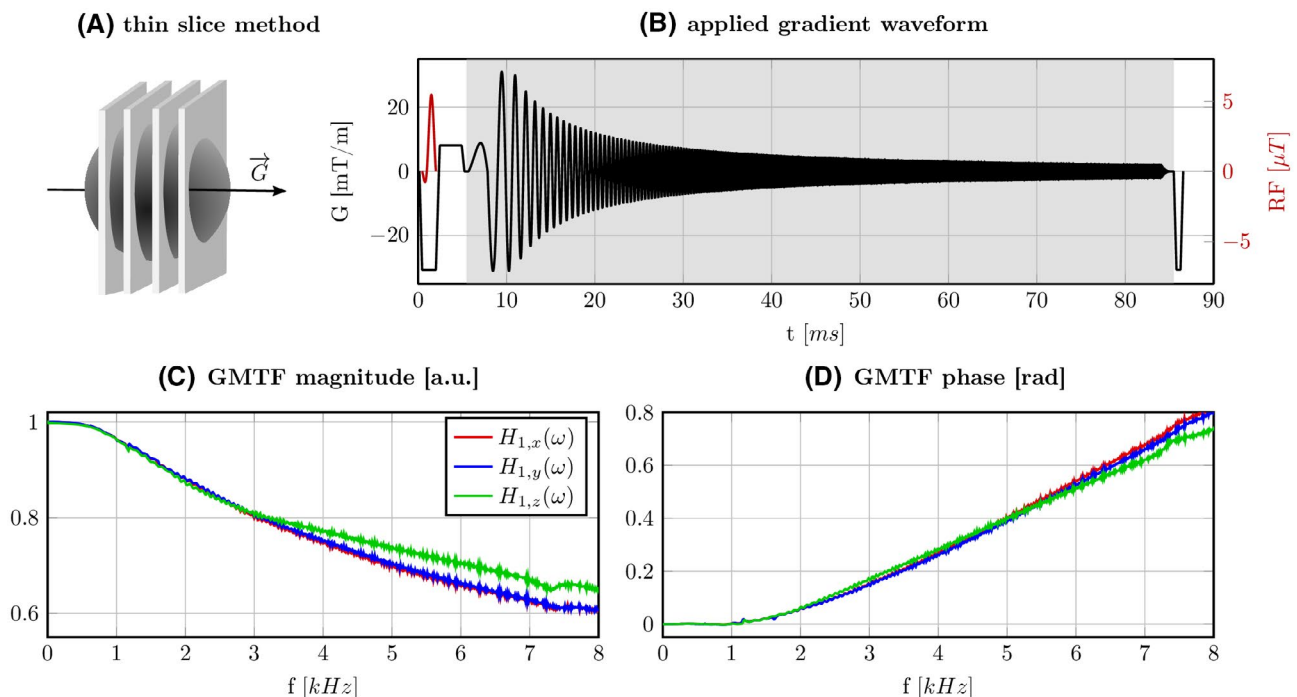

FIGURE 1 Measurement of the GIRF: (A) Schematic diagram of the thin-slice method based on 4 slices per gradient direction. 1D information along the gradient direction is obtained by applying the slice encoding parallel to the measurement direction. (B) The applied chirp gradient waveform in the time domain (black) and the excitation RF pulse (red). The data acquisition window is indicated by the gray background color. (C,D) Measured spectra of the first-order GMTF $H_1(\omega)$. The colors indicate measurements of different gradient directions. Presented are the magnitude and phase in the range of 0 kHz to 8 kHz. GIRF, gradient impulse response function; GMTF, gradient modulation transfer function

was performed in 4 parallel slices located at distances of −26.25 mm, −8.75 mm, 8.75 mm, and 26.25 mm from the iso-center and repeated along all 3 gradient axes (Supporting Information Figure S3A-D). The chirp test gradient response was then calculated using the difference in the phase evolution of the measurements performed with positive and negative readout polarities. The following parameters were used for the GIRF measurement: TR of 2 s; slice thickness of 1.5 mm; 40 averages; sampling dwell time of 1.28 μs; and 62,500 sampling points. The acquisitions of the 4 slices were interleaved and excited during 1 TR. The total scan time required for the acquisition of the GIRF measurement was defined as TR × 40 averages × 2 polarities × 3 directions and was equal to 4 min.

2.2 | UTE pulse sequence and image reconstruction

To measure the signal of tissues with short T_2^* values, a 3D UTE stack-of-stars sequence was employed[45] with a nonselective RF pulse. The excitation was followed by a variable-duration slice encoding gradient and a movable readout gradient. After the sampling of the FID at TE_1, a gradient echo with an opposite gradient readout polarity at TE_2 was acquired (Figure 2A). The FID and the gradient echo were acquired during a single excitation along 1 radial "spoke." An inner loop is defined along the rotation angle and an outer loop along k_z. All spokes within 1 slice were acquired with a uniform, constant azimuthal angle sampling pattern. The minimal FID readout time depended on the RF transmit–receive

switching time of the system. All images were acquired on a 3 Tesla system (Elition X, Philips Medical Systems, Best, the Netherlands).

The GIRF correction was applied as a part of the image reconstruction process.[22,46,47] To this end, the input gradient waveform was convolved with the measured GIRF to predict the real gradient waveform. This convolution can be simplified in the Fourier domain as a multiplication of the Fourier-transformed input gradient waveform with the GMTF. The predicted gradient waveform was used to calculate the k-space positions of the acquired data points. The GIRF correction provided the correction of the whole gradient waveform, including both the FID and the gradient echo.

The nominal correction was based on the default reconstruction of the manufacturer. The nominal gradient waveform applied during FID sampling was calculated by convolving the ideal gradient waveform with a simple, analytic, vendor-parameterized model of the system GMTF. This model was identical for all physical gradient axis. As a result of this convolution the input waveform was slightly smoothed and delayed. Regarding radial gradient echoes, eddy-current induced gradient delays can cause k-space shifts. The used radial acquisition scheme allowed for a simple spoke alignment correction[48]: the signals along spokes with opposed readout directions were correlated in image space to retrieve a phase offset.[49,50] Each spoke was corrected in image space by the estimated linear phase offset, which corresponds to a shift in k-space. The employed k-space spoke alignment for the echoes only shifted the k-space signal and did not affect the sampled k-space locations; therefore, the spoke-aligned gradient waveform is not displayed in Figure 2.
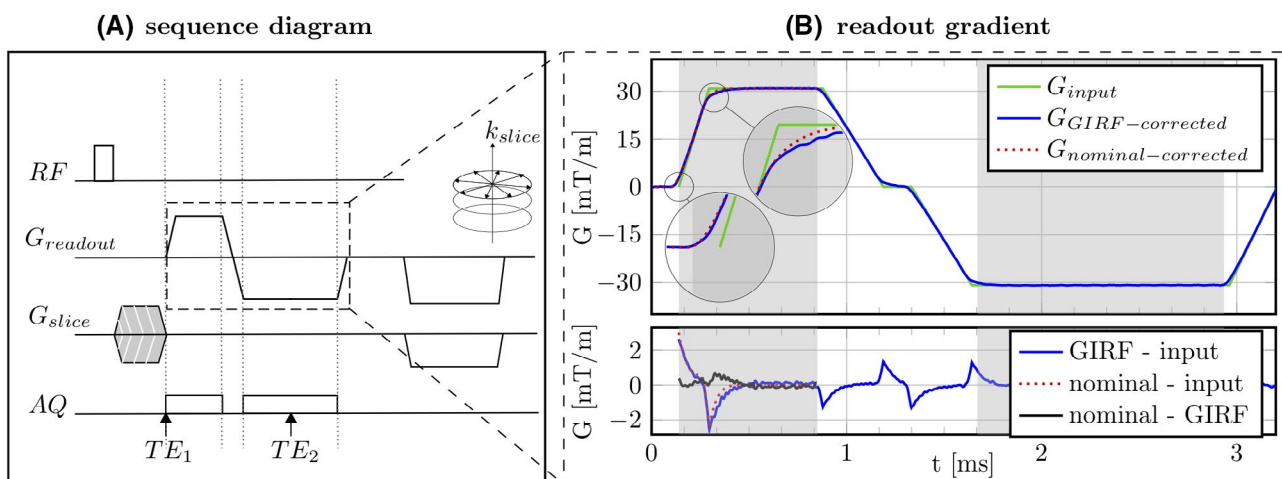

FIGURE 2 UTE stack-of-stars pulse sequence diagram. (A) After the excitation and the 3D time encoding, the FID readout begins at time TE_1, followed by a gradient echo readout with TE_2 using a gradient with opposite polarity to the FID. (B) The whole dual-echo UTE gradient waveform as a function of time after the RF excitation. The gradient echo readout was shifted to achieve a specific TE_2 in which water and fat were in-phase. The data acquisition windows are indicated by the gray background color. Shown are the input gradient waveform G_{input}, GIRF-corrected gradient waveform, and nominal-corrected gradient waveform. In the nominal correction, only the FID readout gradient was corrected, and thus the nominal-corrected gradient was plotted solely for the FID readout. Bottom plot shows the error between the input gradient, GIRF-corrected gradient, and nominal-corrected gradient

For the reconstruction, an image reconstruction toolbox (ReconFrame, Gyrotools, Switzerland) was used to grid the data in 2 dimensions with the corresponding k-space trajectories, to Fourier transform in 3D, and to perform SENSE unfolding in the third Cartesian-sampled dimension. For the gridding, a Kaiser-Bessel kernel was used with a kernel width of 4 k-space sampling steps and a gridder oversampling factor of 1.25. The density was precompensated with weights that were estimated by counting the number of sampling points per ring segment. After the gridding, the image was normalized with the Fourier-transformed kernel function.

2.3 | Phantom measurements

A UTE stack-of-stars, high-resolution dual-echo scan was performed coronally in a phantom with an internal structure. The images were then reconstructed using 2 different trajectories: the nominal- and the GIRF-corrected trajectory. The employed sequence parameters were TE 0.14 ms/ 2.2 ms, TR 7.6 ms, flip angle 5°, in-plane resolution 0.6×0.6 mm^2, slice thickness 1 mm, FOV $210 \times 210 \times 100$ mm^3, dwell time 1.84 μs, ramp length 0.15 ms, maximum gradient strength 30.36 mT/m, acquisition window 0.72 ms, 704 spokes, 393 samples, scan time of 6.15 min, and SENSE acceleration factor of 2 in the Cartesian-sampled dimension.

2.4 | In vivo measurements

In vivo imaging was performed in the knee of a healthy volunteer and in the lumbar spine of 4 patients with spine fractures after informed written consent by each subject and approval by the institutional review board (Klinikum rechts der Isar, Technical University of Munich, Munich, Germany). The spine fracture patients received an MR and a CT scan within 3 days after symptom onset. The CT scans were part of the clinical diagnostic workup.

For the knee measurements, 3D-UTE coronal and sagittal stack-of-stars dual echo measurements were performed with bipolar readout using a 16-channel transmit–receive knee coil and the following parameters: TE 0.14 ms/ 2.2 ms, TR 7.59 ms, flip angle 5°, in-plane resolution 0.6×0.6 mm^2, slice thickness 1 mm, FOV $190 \times 190 \times 164$ mm^3, ramp length 0.15 ms, maximum gradient strength 30.87 mT/m, dwell time 2 μs, acquisition window 0.71 ms, 632 spokes, 355 samples, scan time of 9.2 min, and SENSE acceleration factor of 2 in the Cartesian-sampled dimension. For comparison, a Cartesian T_1-weighted gradient echo was acquired with an equal FOV $190 \times 190 \times 164$ mm^3, equal resolution $0.6 \times 0.6 \times 1.0$ mm^3, equal flip angle 5°, TE 2.3 ms, TR 4.3 ms and a scan time of 2 min,

and SENSE acceleration factor of 2 in the slice encoding dimension. For the subtraction of both echoes a scaling factor was estimated to suppress long T_2 tissue components. A scaling factor of 1.5 gave the best water and fat suppression for a ΔTE of 2.06 ms.

For the spine measurements, a single UTE was acquired using the built-in-table 16-channel posterior coil and the following parameters: TE 0.14 ms, TR 6.3 ms, flip angle 5°, in-plane resolution 0.45×0.45 mm^2, slice thickness 3 mm, FOV $250 \times 250 \times 279$ mm^3, ramp length 0.08 ms, maximum gradient strength 15.04 mT/m, dwell time 3.12 μs, acquisition window 1.77 ms, 945 spokes, 568 samples, radial percentage of 85%, half-scan factor of 0.6 in slice direction, and scan time of 6.3 min.

The nominal and GIRF-corrected UTE spine images were independently read by 2 radiologists. The individual vertebras, L1-L5 and S1, of 3 scanned subjects were scored with a 4-point Likert scale. The radiologists rated the GIRF-corrected and nominal-corrected images with respect to the diagnostic quality of cortical bone visualization from 1 (poor) to 4 (excellent).

2.5 | CT measurements

CT was performed on 1 of 2 CT scanners (Somatom Definition AS+, Siemens Healthineers, and IQon Spectral CT, Philips) with the following parameters according to routine clinical protocols: collimation, 0.6 mm; pixel spacing, 0.4/0.3 mm; pitch factor, 0.8/0.9; tube voltage (peak), 120kV; modulated tube current, 102–132 mA. Images were reformatted in 3 mm slice thickness using a bone-specific convolution kernel (I70H/YB).

3 | RESULTS

3.1 | GIRF measurement results

Figure 1 shows the magnitude and phase of the measured GMTF and depicts the GMTF's low-pass frequency behavior in all 3 axes. Small peaks are visible in the low frequency part of the GMTF, which correspond to mechanical resonances of the gradient coils, for example, at 1.2 kHz. The magnitude of the GMTF for all 3 axes behaved very similarly in the frequency range up to 3 kHz. For frequencies higher than 3 kHz, the x gradient and y gradient had lower transfer ratios than the z gradient, indicating anisotropic eddy current effects. The phase response varied slightly for frequencies of greater than 2 kHz and different gradient directions, indicating a different gradient delay for each axis (Supporting Information Figure S2). The structured noise between 2 kHz to 3 kHz can result from gradient amplifier nonlinearities that distorted the chirp

waveform. The noise in the GMTF measurement increased toward higher frequencies (Supporting Informatoin Figure S3D). Higher frequencies were acquired at the end of the chirp impulse where the gradient strength decreased and the excited signal dropped, which can result in a smaller SNR. The measured GIRF contained information up to a frequency of 10 kHz. The power spectral density of a typical UTE readout gradient showed main contributions in the frequency range below 2 kHz. The integral of the power spectral density reached 95% of the energy after 2 kHz (Figure 3A,B). A comparison of measured gradient waveform and GIRF-predicted gradient waveform showed a good agreement (Figure 3C). There were no systematic changes of the GIRF observed

during repeated measurements over a time span of 1 month (Supporting Information Figure S4).

Figure 2B presents the input waveforms, the nominal-corrected waveforms, and the GIRF-corrected waveforms of the readout gradient as a function of time and after the excitation. The deviations during the FID readout were dominated by short-term effects. There was an increase in the size of deviations from the input gradient waveform during the ramping up of the gradients. Once the plateau was reached, eddy current effects decayed quickly. In comparison, the nominal-corrected gradients and the GIRF-corrected gradients diverged at the very beginning of the FID readout. Regarding the gradient echo readout, there was a short-lived eddy current
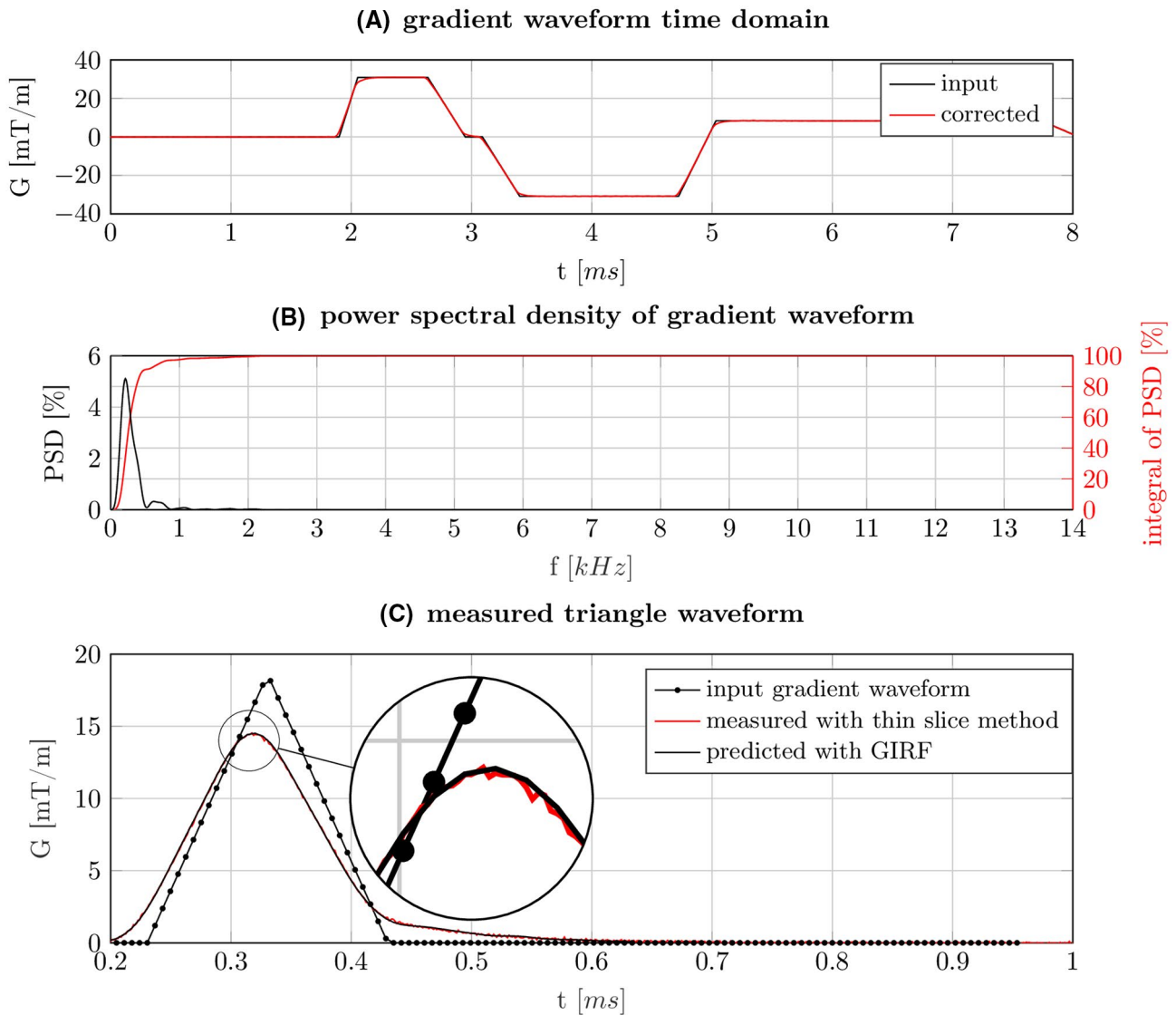

FIGURE 3 (A) typical UTE readout gradient waveform in time domain and (B) its PSD in frequency domain. The measured GMTF based on a chirp test gradient contains information for frequencies up to 10 kHz. The PSD of a typical UTE readout gradient shows main contributions in the frequency range below 2 kHz. The integral of the PSD shows that after 2 kHz, 95% of the energy is reached. (C) Comparison of a measured triangular gradient waveform with the thin slice method, triangular input gradient waveform, and predicted waveform with the GIRF. On the right, the zoomed-in window shows in detail the difference between the GIRF-predicted waveform and the waveform measured with the thin slice measurement for the triangular gradient waveform. PSD, power spectral density

component that was still present at the beginning of the data acquisition window. These deviations at the beginning of the readout resulted in k-space trajectory errors at high frequencies in the radial spoke. Simulations were performed to study the effects of readout gradient waveform deviations on the reconstructed images (Supporting Information Figure S1). The deviations between the GIRF-corrected and nominal-corrected trajectories introduced blurring and an overshoot of signal intensity at object borders between regions with high and low signals.

3.2 | Phantom results

Figure 4 shows UTE images of the structural phantom reconstructed with the nominal-corrected and with the GIRF-corrected k-space trajectories, respectively. Line profiles depict the signal intensity along the white lines and highlight edge artifacts in the nominal-reconstructed images. Using the nominal-corrected gradient waveforms in the reconstruction resulted in an overshoot of the signal at borders between regions with signal and regions without signal. Further, in the nominal-reconstructed images, the halo effect was visible, and high-resolution features were blurred. The halo effect and the blurring were visible particularly at borders between regions with signal and regions without signal. Using the

GIRF-corrected gradient waveforms reduced the hyperintense edge artifacts, minimized the halo effect, and reduced blurring effects. The observed artifacts followed a similar pattern to those in the simulated data.

3.3 | In vivo results

In vivo images of a volunteer's knee joint are shown in Figure 5. Edge artifacts were present at the air–tissue borders in the images reconstructed with nominal-corrected gradients. Edge artifacts were also located near bone–soft-tissue borders. The signal of the cartilage next to the cortical bone was thus overestimated and blurred. Due to the blurring, the thin cortical bone structure was blurred and almost vanished. The aforementioned blurring was removed when the images were reconstructed with the GIRF-corrected trajectories.

Figure 6 shows a radial gradient echo image that was acquired after a UTE-FID readout and compares it to a Cartesian gradient echo image. The radial images were reconstructed by applying a k-space spoke alignment and using the GIRF-corrected gradient waveforms. The use of the GIRF-corrected gradient waveforms improved the contrast, enhanced the homogeneity, and achieved a better agreement of the signal variation with the Cartesian reference scan. In Figure 7, the radial gradient echoes were compared with the
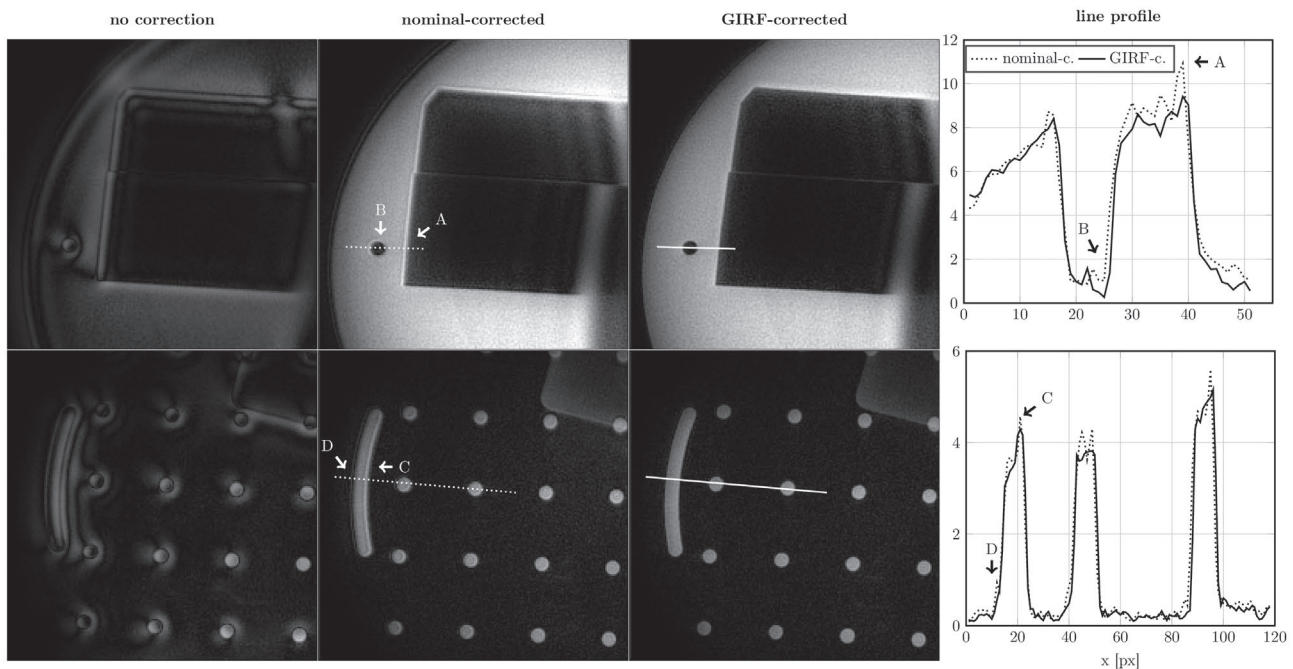

FIGURE 4 UTE stack-of-stars images of a structural phantom that was scanned coronally. The phantom images were reconstructed using noncorrected, nominal-corrected, and GIRF-corrected trajectories. Line profiles depict the signal intensity along the white lines shown on the left. Artifacts are highlighted by arrows. The use of the nominal-corrected trajectories in the reconstruction resulted in edge artifacts. At borders between regions with signal and regions without signal (arrows A and C), the signal showed overshoots and formed hyperintense edges. As compared with the GIRF-corrected images, the nominal-corrected images showed a higher signal in the regions without signal (arrows B and D) and blurred high-resolution features
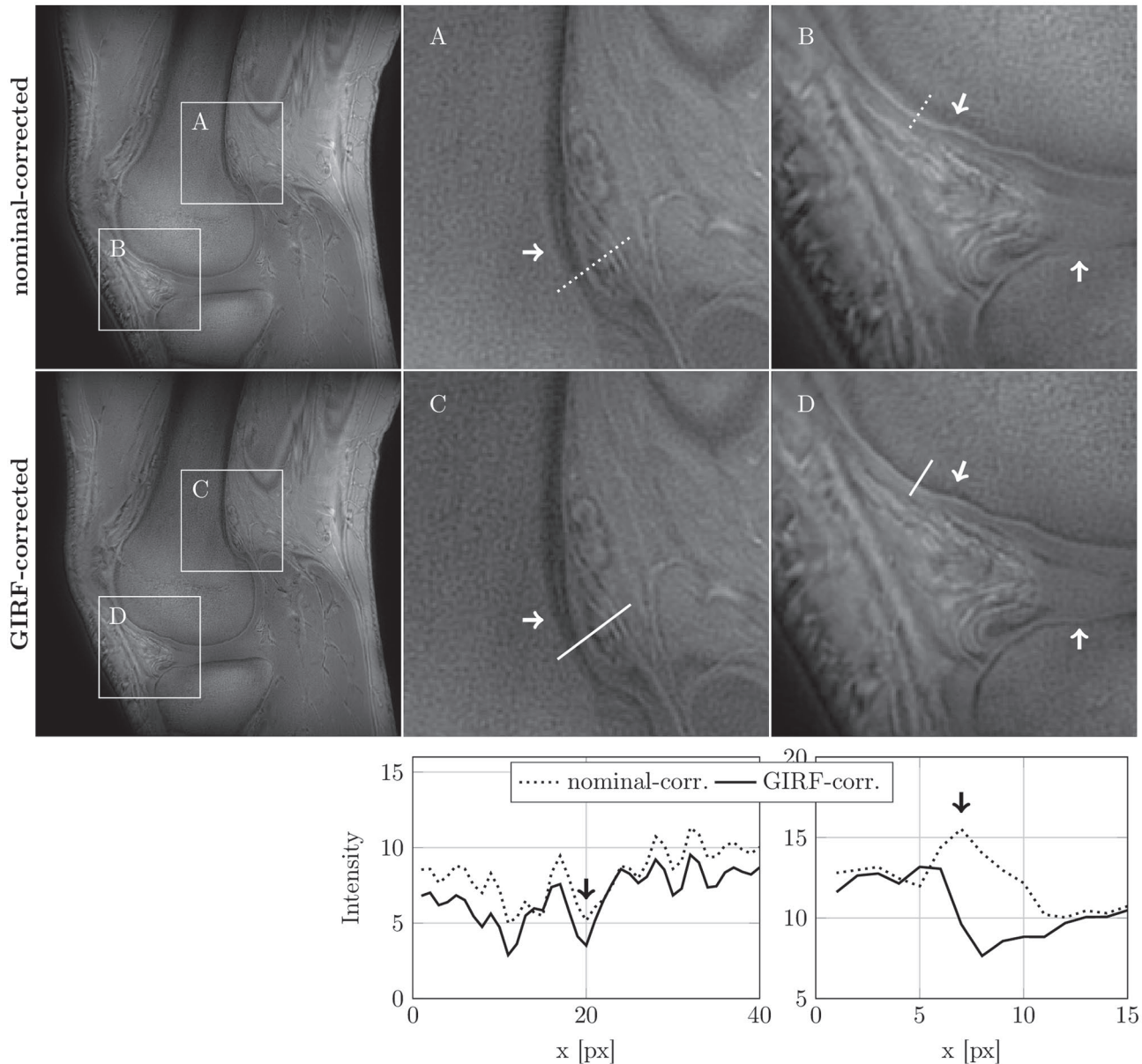
FIGURE 5 In vivo UTE sagittal knee images with the Cartesian-encoded dimension being perpendicular to the shown slices. The UTE images were reconstructed using the nominal gradient waveforms and the GIRF-corrected waveforms. Line profiles depict the signal intensity along the white lines shown in the presented image. White arrows in the images and black arrows in the line plots highlight regions where thin cortical bone structures are blurred. In comparison to (A), the cortical bone shows higher contrast and appears slightly thinner in (C). In (B) the thin cortical bone at the cartilage border is barely visible, whereas the deep cartilage appears exaggerated and blurred. In (D), the cortical bone and the deep articular cartilage are sharper and better depictable

FID images of the same scan. The difference map highlights edge artifacts in the images reconstructed using the nominal-corrected trajectory for the FID and the k-space spoke alignment for the echo. Thin cortical bone structures were blurred and misclassified as soft tissue when not using the GIRF-corrected trajectories.

Figure 8 shows an in vivo sagittal lumbar spine UTE image of a patient with a spine fracture, reconstructed using nominal-corrected and GIRF-corrected gradient waveforms. The upper row of Figure 8 presents the reconstructed full-FOV with the natural contrast, whereas the contrast was inverted in the

bottom row of Figure 8 so that bone appears bright for a better visual comparison with the CT image. The CT and MRI data were manually coregistered in 3D with respect to the vertebra indicated by the blue cross. In the nominal-reconstructed UTE images, thin bone structures appeared bright in the natural contrast and were misclassified as soft-tissue because high-resolution features were blurred. The shape of the vertebra was better visualized with the GIRF-corrected reconstruction.

Figure 9 compares UTE images and CT images of 3 patients with spine fractures using zoomed-in sagittal slices of the lumbar spine. The contrast of the MR images was inverted
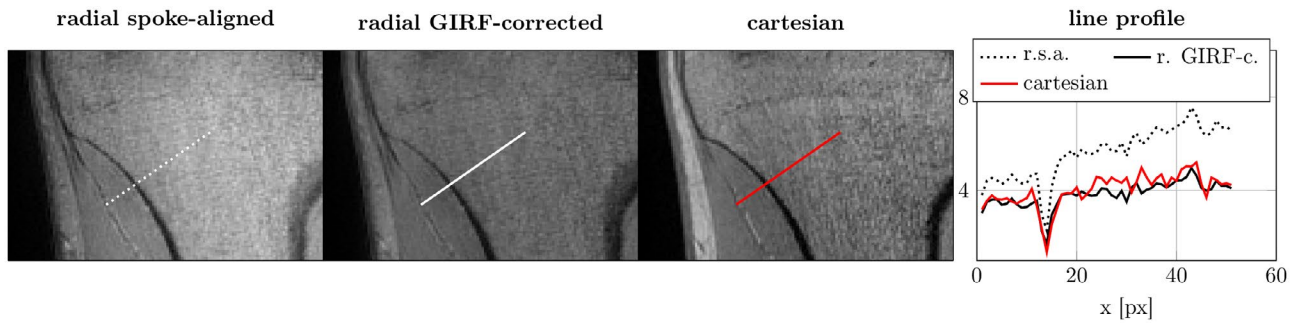
FIGURE 6 In vivo radial and Cartesian gradient echo knee images. The radial gradient echo was acquired after a UTE-FID readout with an opposite gradient polarity to that of the UTE-FID readout. The images were reconstructed by applying k-space spoke alignment and with the GIRF-corrected gradient waveforms. A Cartesian gradient echo with the same TE was acquired for comparison. The line profile depicts the signal amplitude along the lines presented on the left. The contrast, homogeneity, and agreement between radial and Cartesian signal were improved by means of the GIRF-corrected gradient waveforms
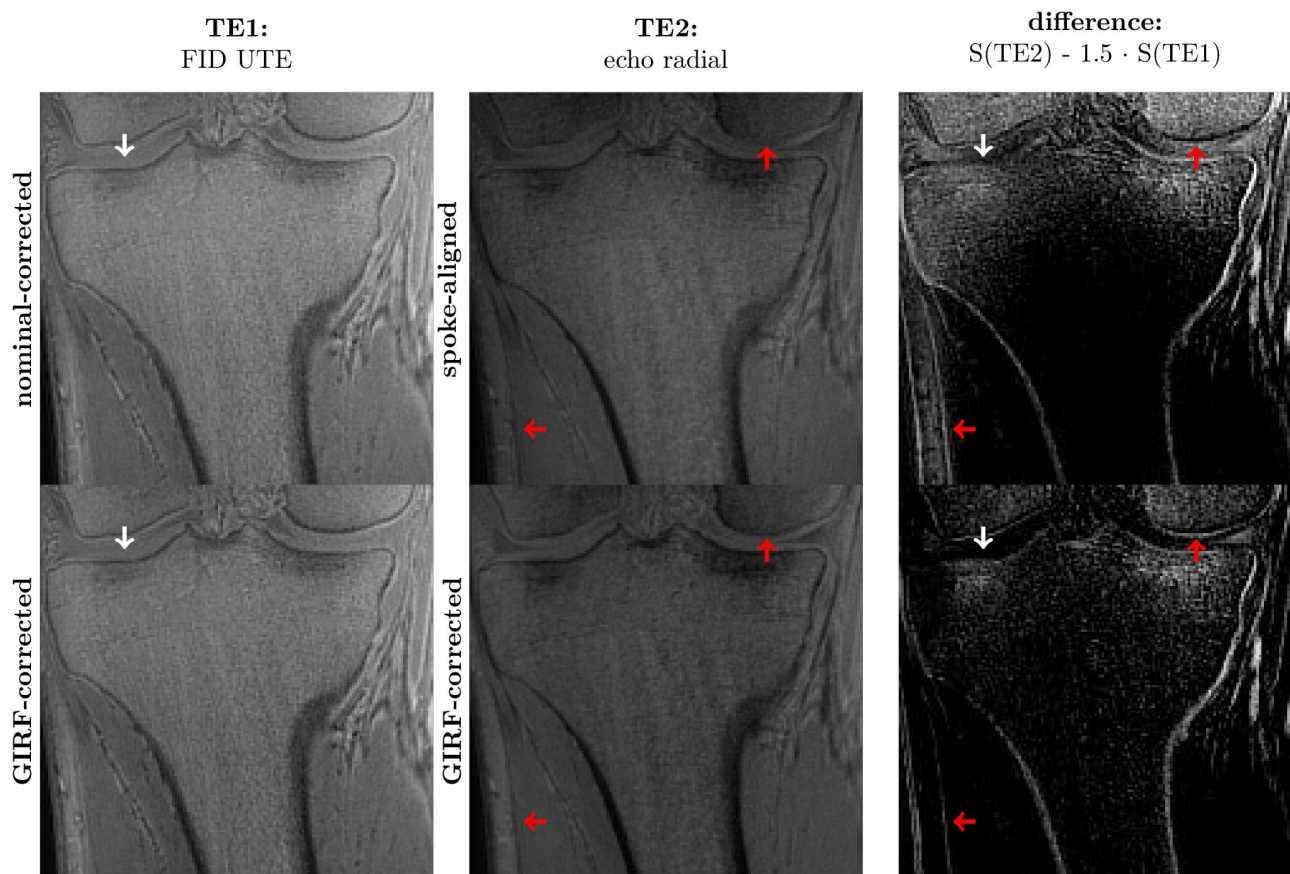

FIGURE 7 In vivo UTE dual-echo knee images. Upper row: FID corrected with the nominal-corrected gradient waveforms, radial gradient echo image reconstructed after k-space spoke alignment, and the difference of the signals. Bottom row: Same as in the top row albeit with FID and radial gradient echo reconstructed with GIRF-corrected gradient waveforms. White and red arrows highlight improvements due to the GIRF-correction in the FID-UTE and the radial gradient echo images, respectively. In the nominal-reconstructed UTE and the k-space spoke aligned radial gradient echo images, high-resolution features were blurred. In the difference maps, these thin blurred structures disappeared and bone was misclassified as soft tissue. Further, the k-space spoke aligned radial gradient echo images appeared inhomogeneous, which is leading to a misclassification of soft tissue as bone. The GIRF-correction improved both the FID images and radial gradient echo images, reduced blurring, and amended the homogeneity

such that bone appears bright. In all scans, the image quality was improved using the GIRF-corrected gradient waveforms. The images were less blurry, had higher contrast, and the bone

structures became more visible when using GIRF-corrected versus nominal-corrected gradients. The shape of the vertebra in the GIRF-corrected images matched the shape of the
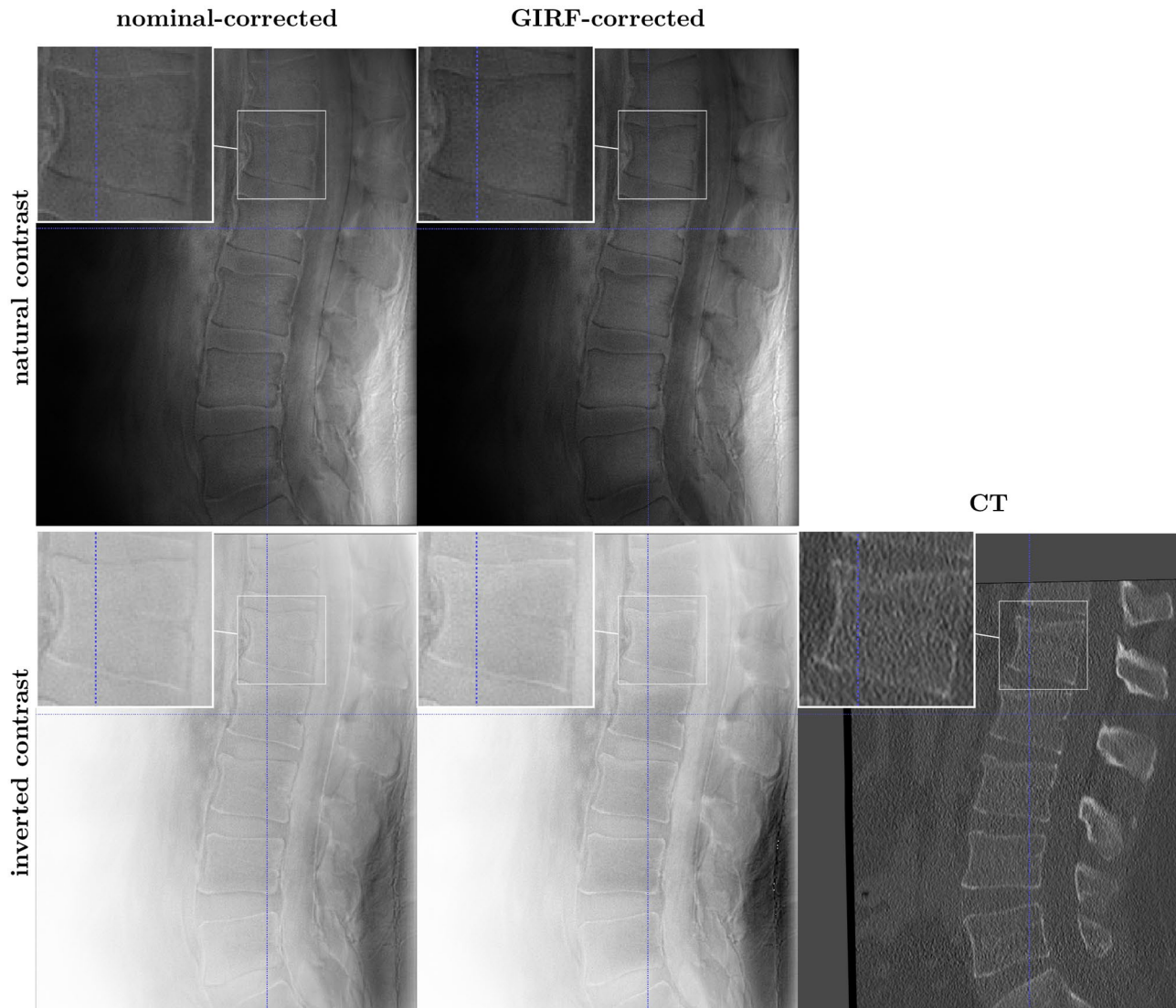
FIGURE 8 In vivo UTE lumbar spine sagittal images of a patient with a spine fracture. The UTE images were reconstructed using the nominal-corrected gradient waveforms and GIRF-corrected waveforms. Upper row: the full FOV with the natural contrast. Bottom row: same as the upper row but the contrast was inverted for comparison with the CT image. The CT and MRI data were manually coregistered in 3D at the point indicated by the blue cross. In the nominal-reconstructed UTE images, high-resolution features were blurred. Thin bone structures appeared bright and were misclassified as soft tissue. The improvements due to the GIRF-corrected reconstruction made it easier to determine the shape of the vertebra

vertebra in the CT scans. In the nominal-corrected images, the thin bone structures were blurred, and the contrast could change from bright to dark in the inverted images, leading to the misclassification of bone as soft tissue or connective tissue. The rating of the diagnostic quality of the cortical bone visualization showed significant better results for the GIRF-corrected images than for the nominal corrected images and a high agreement among the readers. The median and SD scores of the rating for the GIRF-corrected images were 3.17 ± 0.79 (good) for the first reader and 3.28 ± 0.83 (good) for the second reader. The diagnostic quality of the nominal-corrected images was rated significantly lower than the GIRF-corrected images, with scores equal to 1.78 ± 0.64 (moderate) for the first reader and 1.83 ± 0.70 (moderate) for the second reader.

4 | DISCUSSION

Gradient chain miscalibration-induced artifacts are known to lead to errors in UTE MRI sequences, and it has been shown that eddy current and delay effects can be corrected for by measuring the k-space trajectories. This work demonstrated that, with a GIRF measured using the standard scanner hardware, the image quality of radial UTE images can be reliably improved. It was shown that the reduction of blurring and artifacts is especially crucial in high-resolution MSK imaging of thin bone structures and thin connective tissues. Without the GIRF-corrected reconstruction, such thin bone structures disappear or can become even misclassified as soft tissue. The improvements of a correction based on a GIRF
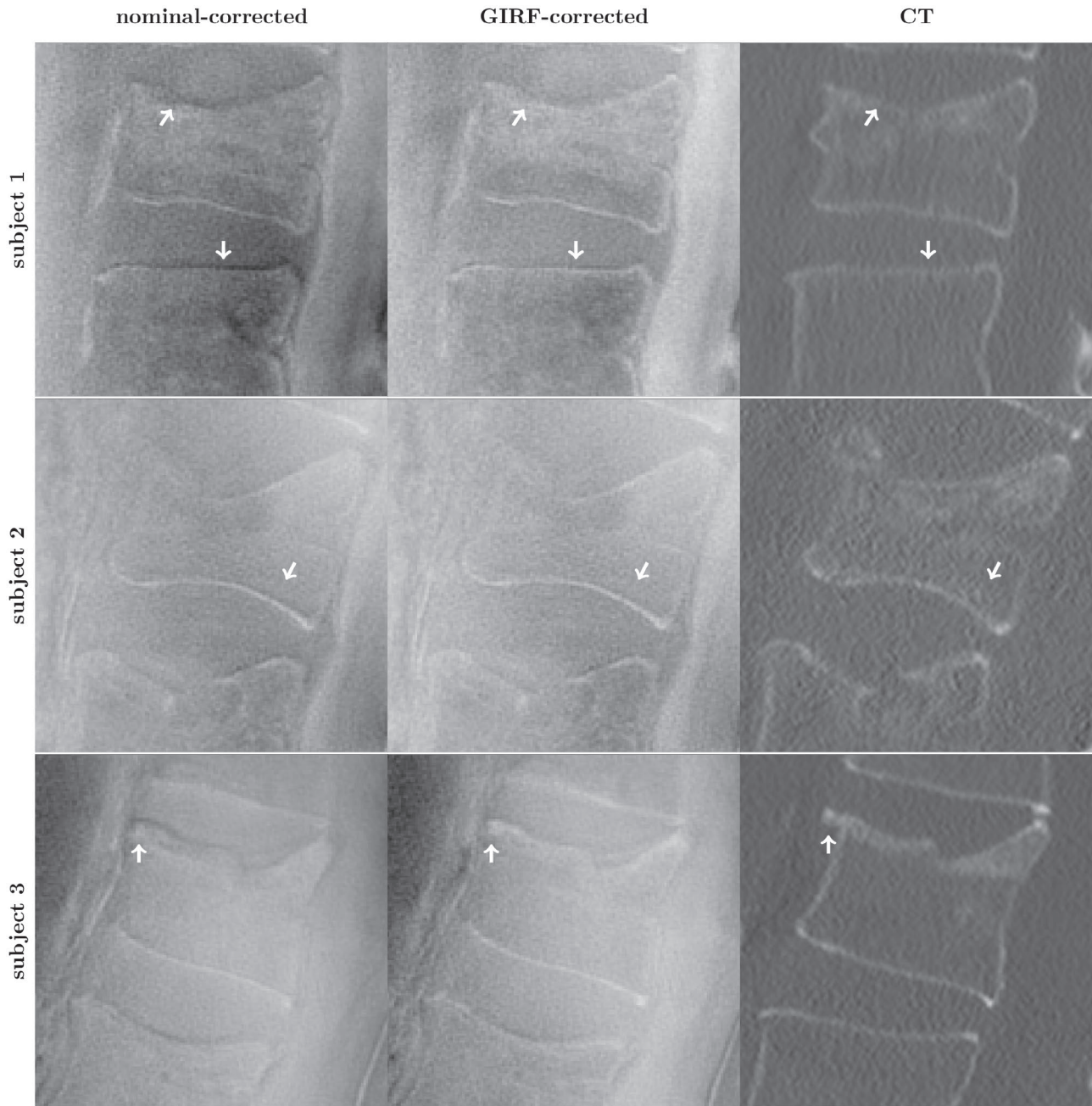
nominal-corrected	GIRF-corrected	CT

FIGURE 9   In vivo UTE lumbar spine sagittal images of 3 patients with spine fractures. The contrast of the MR images was inverted such that bone appears bright. White arrows highlight improvements achieved with the GIRF-correction. In subject 1, thin bone structures appeared dark in the nominal-corrected images where a bright bone was expected as compared with the CT images. In subject 2, the vertebral body appeared blurred and with a less contrast in the nominal- versus the GIRF-corrected images. Subject 3 showed a sclerotic zone as a result of the fresh vertebral fracture. Once again, in comparison with the CT, areas with expected high signals appeared dark in the nominal-corrected images. In all scans, the image quality was improved using the GIRF-corrected gradient waveforms. In comparison with the CT images, the shapes of the vertebrae were depicted better in the GIRF-corrected images

acquired in a simple phantom scan were presently verified with phantom and in vivo measurements. The results not only reproduced prior reported improvements to UTE trajectory-correction methods for reducing both undershoot and overshoot of signal intensity at object–background borders but primarily highlighted the need of k-space trajectory correction in high-resolution UTE imaging.

Typically, eddy current correction methods measure directly the gradient with specialized NMR field probes,[21,23,33,51] perform separate calibration scans,[24,30,52,53] or extract information directly from the measured raw data without any additional calibration scans.[31,32,54] It was also previously reported that eddy currents can be corrected by measuring a transfer function to describe the gradient

characteristics.[22,38,47,55] Eddy current correction in the context of UTE imaging was done before by measuring the UTE gradient waveforms for a fixed parameter set with specialized NMR field probes[33] and by running calibration scans in a phantom before the actual measurements were performed.[17,36,42] The proposed GIRF measurement showed that the use of a chirp-based LTI model[22,24,47] is able to provide a transfer function that improves the reconstruction of UTE images independently of imaging parameters and required no additional hardware. The spectrum of the chirp waveform covered a large frequency range without blind spots and with high spectral density (12.5 Hz) and enabled a fast measurement (4 min) when compared to triangular input functions. However, at low frequencies (< 100 Hz), the chirp's spectral density approached 0, leading to a diverging intensity in the spectrum of the GIRF.[56] The proposed GIRF-based correction method for eddy-current correction has the advantage that only a 1-time calibration scan is needed, and the measured transfer function can be used in all subsequent image reconstructions. The measured GIRF indicates anisotropic eddy-current behavior that depends upon the gradient axis. No gradient terms of a second- or higher-order were measured with the phantom-based method, whereas such higher-order terms could be derived based on a field camera[38,46] or from a 3D phantom based approach using phase encoding.[40]

The performed simulations and phantom measurements investigated artifacts on the reconstructed images, originating from the readout gradient waveform deviations, including blurring, changes in background signal, and emphasized edge effects. An important aspect of the simulations was the introduction of a gradient delay to the low-pass model-based correction method. Approaches determining a single delay are widely used for radial acquisition schemes, for which the sampling is performed on the flat top of a trapezoidal gradient. The simulations showed that the simple model with an additional gradient delay is not sufficient as a k-space trajectory correction method for high-resolution UTE imaging. In addition, the simulations showed that the GIRF correction accounts for the dependence of the response on the readout gradient axis, whereas the model-based correction method cannot easily account for such effects. To obtain the best reconstruction result the accurate gradient waveform is needed with an exactly calibrated delay. The GIRF correction method is model-independent and requires no manual delay optimization. The analysis of the phantom experiments reproduced previously simulated artifacts such as blurring, background signal, and edge enhancement. All of these artifacts were reduced using the GIRF-corrected gradient waveforms, indicating that the GIRF-corrected gradient waveforms comprise important features of the real gradient waveforms such as the delay and the axis-dependent gradient shape. To summarize, the GIRF correction method is based on the transfer function

of the entire gradient system and thus describes better than any other correction models its behavior, thus allowing a better prediction of the k-space deviations induced by the gradients in UTE imaging.

In vivo, the GIRF correction was applied to high-resolution UTE images, showing the improvements for thin tissues in the knee such as cortical bone and cartilage. Further, the GIRF correction was applied to the FID-echo readout with opposite gradient polarities for the FID and the gradient echo. The correction of FID and gradient echo k-space trajectories were performed in 1 step. Conversely, traditional correction methods include 2 steps for the reconstruction of UTE–multi-echo data and correct the FID (using the nominal correction) and radial gradient echo data (using the k-space spoke alignment) separately. Such traditional correction methods can become slower and can lead to inconsistencies in the signal amplitude between the FID and the echo. Gradient waveform deviations can additionally lead to geometric distortions such as stretching and shifting. The GIRF correction treats FIDs and echoes in the same way. The GIRF-based correction method is therefore important if FIDs, and radial echoes are supposed to be matched, for example, to subtract both images to get rid of long T_2^* components and to highlight short T_2^* components.

The comparison of UTE in vivo spine images with CT images highlighted the importance of a GIRF-based correction method of UTE images for high-resolution features. Gradient waveform deviations can blur thin bone structures and fine connective tissues. Overestimated edges can lead to the misclassification of bone as soft tissue. The proposed methodology could therefore be particularly useful first for UTE CT-like imaging[57] or attenuation correction for PET/MRI,[33,58] where UTE sequences have been proposed to help to distinguish between cortical bone and air. Second, the proposed methodology could be useful for generating high-quality UTE-based CT-like images for diagnostic musculoskeletal imaging, especially in the evaluation of bone changes. MR-based CT-like imaging has been recently proposed, aiming at reducing the radiation burden on the patient, avoiding the need to perform additional X-ray and CT imaging when MR is already part of clinical care,[59] and achieving a hybrid contrast.[60] To further improve the image contrast of UTE imaging of bone structures, long T_2 components could be further suppressed by employing inversion recovery and fat saturation techniques.[61,62]

The proposed correction method was shown to be beneficial not only in high-resolution single-echo UTE imaging but also in dual-echo imaging. Therefore, our results might imply a level of importance of the gradient corrections when UTE sequences are employed for UTE multi-echo imaging that acquires more than 1 TE per TR. Further, correcting the UTE trajectories could also be beneficial in the context of quantitative T_2^* measurements of short T_2^* tissues when employing

UTE multi-echo imaging and acquiring more than 1 TE per TR.[62]

The present work has several limitations: First, the present work does not address the effect of B_0 eddy currents, which may promote unwanted phase accumulation of the sampled signal. We expect the effect to be small in UTE imaging because the k-space center is initially measured. However, because the B_0 transfer function can be extracted from the acquired GIRF data, this correction could be readily implemented. Second, the measured GIRF contained information up to a frequency of 10 kHz. This is sufficient for typical UTE readout gradient waveforms yet may not be sufficient for arbitrary gradient waveforms. Third, the proposed correction method requires that the reconstruction is able to use the predicted trajectories in order to produce the corrected images. Therefore, an interface for providing the corrected trajectory to the gridding algorithm or the use of a custom-designed image reconstruction framework is required. Fourth, the GIRF-based correction method requires the precise knowledge of the input gradient waveforms in order to predict the real gradient waveform. Such knowledge may not be accessible for all vendor-specific sequences. The increased reconstruction complexity and the need of input waveforms to perform the correction might affect the future adoption of the GIRF-based correction method. Fifth, the presented CT-like images of the cortical bone in the lumbar spine by inverting the contrast of UTE images could be confounded by the fact that the UTE images are T_2^*-weighted, T_1-weighted, and proton density-weighted. This mixed weighting of UTE images could affect the ability of inverting the contrast of UTE images in resolving bone structures at least at the presently used parameters (TE, TR, and flip angle). Zero TE sequences have been recently used for CT-like imaging of bone structures by inverting the contrast of zero TE images, which have been considered to be primarily proton density-weighted.[60,63,64] The inversion of the contrast of UTE images was presently shown as only an example of the effect of UTE trajectory correction on a clinically relevant, high-resolution MSK imaging setting. The ability of inverted UTE images for CT-like bone imaging in the lumbar spine requires further investigation. Finally, the GIRF-based correction method does not adapt geometric distortions caused by spatial nonlinearities in the gradient fields at the edge of the FOV. These nonlinearities are static and do not account for dynamic trajectory errors from eddy currents.

5 | CONCLUSION

A simple phantom-based GIRF measurement and standard MRI scanner hardware were used to estimate k-space trajectories for high-resolution UTE MSK imaging, and in particular to improve cortical bone visualization. It was demonstrated that the correction based on the measured GIRF minimizes artifacts due to gradient waveform distortions in comparison with a model-based trajectory correction method representing a typical implementation on a clinical system.

CONFLICT OF INTEREST
The authors PB and JR are employed by Philips GmbH Innovative Technologies.

ORCID
Sophia Kronthaler https://orcid.org/0000-0001-7913-1238
Jürgen Rahmer https://orcid.org/0000-0001-8514-4801

REFERENCES
1. Gatehouse PD, Bydder GM. Magnetic resonance imaging of short T2 components in tissue. *Clin Radiol*. 2003;58:1-19.
2. Robson MD, Gatehouse PD, Bydder M, Bydder GM. Magnetic resonance: An introduction to ultrashort TE (UTE) imaging. *J Comput Assist Tomogr*. 2003;27:825-846.
3. Weiger M, Pruessmann KP. Short-T2 MRI: Principles and recent advances. *Prog Nucl Magn Reson Spectrosc*. 2019;114-115:237-270.
4. Pauli C, Bae WC, Lee M, et al. Ultrashort-echo time MR imaging of the patella with bicomponent analysis: Correlation with histopathologic and polarized light microscopic findings. *Radiology*. 2012;264:484-493.
5. Gatehouse PD, He T, Puri BK, Thomas RD, Resnick D, Bydder GM. Contrast-enhanced MRI of the menisci of the knee using ultrashort echo time (UTE) pulse sequences: Imaging of the red and white zones. *Br J Radiol*. 2004;77:641-647.
6. Hodgson RJ, O'Connor PJ, Grainger AJ. Tendon and ligament imaging. *Br J Radiol*. 2012;85:1157-1172.
7. Du J, Bydder GM. Qualitative and quantitative ultrashort-TE MRI of cortical bone. *NMR Biomed*. 2013;26:489-506.
8. Chang EY, Du J, Chung CB. UTE imaging in the musculoskeletal system. *J Magn Reson Imaging*. 2015;41:870-883.
9. Robson MD, Bydder GM. Clinical ultrashort echo time imaging of bone and other connective tissues. *NMR Biomed*. 2006;19:765-780.
10. Qian Y, Williams AA, Chu CR, Boada FE. High-resolution ultrashort echo time (UTE) imaging on human knee with AWSOS sequence at 3.0 T. *J Magn Reson Imaging*. 2012;35:204-210.
11. Bae WC, Dwek JR, Znamirowski R, et al. Ultrashort echo time MR imaging of osteochondral junction of the knee at 3 T: Identification of anatomic structures contributing to signal intensity. *Radiology*. 2010;254:837-845.
12. Eckstein F, Glaser C. Measuring cartilage morphology with quantitative magnetic resonance imaging. *Semin Musculoskelet Radiol*. 2004;8:329-353.

13. Foreman SC, Ashmeik W, Baal JD, et al. Patients with type 2 diabetes exhibit a more mineralized deep cartilage layer compared with nondiabetic controls: A pilot study. *Cartilage*. 2019. https://doi.org/10.1177/1947603519870853

14. Ritzel H, Amling M, Posl M, Hahn M, Delling G. The thickness of human vertebral cortical bone and its changes in aging and osteoporosis: A histomorphometric analysis of the complete spinal column from thirty-seven autopsy specimens. *J Bone Miner Res*. 1997;12:89-95.

15. Johnson EM, Vyas U, Ghanouni P, Pauly KB, Pauly JM. Improved cortical bone specificity in UTE MR imaging. *Magn Reson Med*. 2017;77:684-695.

16. Lee H, Zhao X, Song HK, Zhang R, Bartlett SP, Wehrli FW. Rapid dual-RF, dual-echo, 3D ultrashort echo time craniofacial imaging: A feasibility study. *Magn Reson Med*. 2019;81:3007-3016.

17. Takizawa M, Hanada H, Oka K, Takahashi T, Yamamoto E, Fujii M. A robust ultrashort TE (UTE) imaging method with corrected k-space trajectory by using parametric multiple function model of gradient waveform. *IEEE Trans Med Imaging*. 2013;32:306-316.

18. Van Vaals JJ, Bergman AH. Optimization of eddy-current compensation. *J Magn Reson*. 1990;90:52-70.

19. Brodsky EK, Samsonov AA, Block WF. Characterizing and correcting gradient errors in non-cartesian imaging: Are gradient errors linear time-invariant (LTI)? *Magn Reson Med*. 2009;62:1466-1476.

20. Bernstein MA, King KF, Zhou XJ. *Handbook of MRI Pulse Sequences*. Burlington, MA: Elsevier; 2004.

21. De Zanche N, Barmet C, Nordmeyer-Massner JA, Pruessmann KP. NMR probes for measuring magnetic fields and field dynamics in MR systems. *Magn Reson Med*. 2008;60:176-186.

22. Liu H, Matson GB. Accurate measurement of magnetic resonance imaging gradient characteristics. *Materials (Basel)*. 2014;7:1-15.

23. Dietrich BE, Brunner DO, Wilm BJ, et al. A field camera for MR sequence monitoring and system analysis. *Magn Reson Med*. 2016;75:1831-1840.

24. Addy NO, Wu HH, Nishimura DG. Simple method for MR gradient system characterization and k-space trajectory estimation. *Magn Reson Med*. 2012;68:120-129.

25. Mason GF, Harshbarger T, Hetherington HP, Zhang Y, Pohost GM, Twieg DB. A method to measure arbitrary k-space trajectories for rapid MR imaging. *Magn Reson Med*. 1997;38:492-496.

26. Takahashi A, Peters T. Compensation of multi-dimensional selective excitation pulses using measured k-space trajectories. *Magn Reson Med*. 1995;34:446-456.

27. Harkins KD, Does MD, Grissom WA. Iterative method for predistortion of MRI gradient waveforms. *IEEE Trans Med Imaging*. 2014;33:1641-1647.

28. Alley MT, Glover GH, Pelc NJ. Gradient characterization using a Fourier-transform technique. *Magn Reson Med*. 1998;39:581-587.

29. Jang H, McMillan AB. A rapid and robust gradient measurement technique using dynamic single-point imaging. *Magn Reson Med*. 2017;78:950-962.

30. Duyn JH, Yang Y, Frank JA, van der Veen JW. Simple correction method for k-space trajectory deviations in MRI. *J Magn Reson*. 1998;132:150-153.

31. Deshmane A, Blaimer M, Breuer F, et al. Self-calibrated trajectory estimation and signal correction method for robust radial imaging using GRAPPA operator gridding. *Magn Reson Med*. 2016;75:883-896.

32. Kramer M, Biermann J, Reichenbach JR. Intrinsic correction of system delays for radial magnetic resonance imaging. *Magn Reson Imaging*. 2015;33:491-496.

33. Aitken AP, Giese D, Tsoumpas C, et al. Improved UTE-based attenuation correction for cranial PET-MR using dynamic magnetic field monitoring. *Med Phys*. 2014;41:012302.

34. Herrmann KH, Kramer M, Reichenbach JR. Time efficient 3D radial UTE sampling with fully automatic delay compensation on a clinical 3T MR scanner. *PLoS One*. 2016;11:e0150371.

35. Magland JF, Saligheh-Rad H, Wehrli FW. Correcting for gradient imperfections in ultra-short echo time imaging. In Proceedings of the 18th Scientific Meeting of ISMRM, Sweden, Stockholm, 2010. Abstract 3102.

36. Atkinson IC, Lu A, Thulborn KR. Characterization and correction of system delays and eddy currents for MR imaging with ultrashort echo-time and time-varying gradients. *Magn Reson Med*. 2009;62:532-537.

37. Latta P, Starcuk Z Jr, Gruwel ML, Weber MH, Tomanek B. K-space trajectory mapping and its application for ultrashort echo time imaging. *Magn Reson Imaging*. 2017;36:68-76.

38. Vannesjo SJ, Haeberlin M, Kasper L, et al. Gradient system characterization by impulse response measurements with a dynamic field camera. *Magn Reson Med*. 2013;69:583-593.

39. Brodsky EK, Klaers JL, Samsonov AA, Kijowski R, Block WF. Rapid measurement and correction of phase errors from B0 eddy currents: Impact on image quality for non-Cartesian imaging. *Magn Reson Med*. 2013;69:509-515.

40. Rahmer J, Mazurkewitz P, Bornert P, Nielsen T. Rapid acquisition of the 3D MRI gradient impulse response function using a simple phantom measurement. *Magn Reson Med*. 2019;82:2146-2159.

41. Gurney P, Pauly JM, Nishimura DG. A Simple Method for Measuring B0 Eddy Currents. In Proceedings of the 13th Annual Meeting of ISMRM, Miami, Florida, 2005. Abstract 866.

42. Zhao X, Lee H, Song HK, Cheng CC, Wehrli FW. Impact of gradient imperfections on bone water quantification with UTE MRI. *Magn Reson Med*. 2020;84:2034-2047.

43. Lee H, Zhao X, Song HK, Wehrli FW. Self-navigated three-dimensional ultrashort echo time technique for motion-corrected skull MRI. *IEEE Trans Med Imaging*. 2020;39:2869-2880.

44. Prince JL, Links JM. *Medical Imaging Signals and Systems*. Upper Saddle River, NJ: Pearson Prentice Hall; 2006.

45. Qian Y, Boada FE. Acquisition-weighted stack of spirals for fast high-resolution three-dimensional ultra-short echo time MR imaging. *Magn Reson Med*. 2008;60:135-145.

46. Vannesjo SJ, Graedel NN, Kasper L, et al. Image reconstruction using a gradient impulse response model for trajectory prediction. *Magn Reson Med*. 2016;76:45-58.

47. Campbell-Washburn AE, Xue H, Lederman RJ, Faranesh AZ, Hansen MS. Real-time distortion correction of spiral and echo planar images using the gradient system impulse response function. *Magn Reson Med*. 2016;75:2278-2285.

48. Ruschke S, Eggers H, Kooijman H, et al. Correction of phase errors in quantitative water-fat imaging using a monopolar time-interleaved multi-echo gradient echo sequence. *Magn Reson Med*. 2017;78:984-996.

49. Block KT, Uecker M. Simple method for adaptive gradient-delay compensation in radial MRI. In Proceedings of the 19th Annual Meeting of ISMRM, Montréal, Québec, Canada, 2011. Abstract 2816.

50. Untenberger M, Tan Z, Voit D, et al. Advances in real-time phase-contrast flow MRI using asymmetric radial gradient echoes. *Magn Reson Med*. 2016;75:1901-1908.

51. Vannesjo SJ, Dietrich BE, Pavan M, et al. Field camera measurements of gradient and shim impulse responses using frequency sweeps. *Magn Reson Med*. 2014;72:570-583.

52. Robison RK, Devaraj A, Pipe JG. Fast, simple gradient delay estimation for spiral MRI. *Magn Reson Med*. 2010;63:1683-1690.

53. Beaumont M, Lamalle L, Segebarth C, Barbier EL. Improved k-space trajectory measurement with signal shifting. *Magn Reson Med*. 2007;58:200-205.

54. Lee KJ, Paley MN, Griffiths PD, Wild JM. Method of generalized projections algorithm for image-based reduction of artifacts in radial imaging. *Magn Reson Med*. 2005;54:246-250.

55. Stich M, Wech T, Slawig A, et al. Gradient waveform pre-emphasis based on the gradient system transfer function. *Magn Reson Med*. 2018;80:1521-1532.

56. Mazurkewitz P, Rahmer J, Börnert P. GIRF measurement using a combination of triangular and chirp waveform input functions. In Proceedings of the 26th Annual Meeting of ISMRM, Paris, France, 2018. Abstract 0169.

57. Johansson A, Karlsson M, Yu J, Asklund T, Nyholm T. Voxelwise uncertainty in CT substitute derived from MRI. *Med Phys*. 2012;39:3283-3290.

58. Keereeman V, Fierens Y, Broux T, De Deene Y, Lonneux M, Vandenberghe S. MRI-based attenuation correction for PET/MRI using ultrashort echo time sequences. *J Nucl Med*. 2010;51:812-818.

59. Gersing AS, Bodden J, Neumann J, et al. Accelerating anatomical 2D turbo spin echo imaging of the ankle using compressed sensing. *Eur J Radiol*. 2019;118:277-284.

60. Argentieri EC, Koff MF, Breighner RE, Endo Y, Shah PH, Sneag DB. Diagnostic accuracy of zero-echo time MRI for the evaluation of cervical neural foraminal stenosis. *Spine (Phila Pa 1976)* 2018;43:928-933.

61. Carl M, Bydder GM, Du J. UTE imaging with simultaneous water and fat signal suppression using a time-efficient multispoke inversion recovery pulse sequence. *Magn Reson Med*. 2016;76:577-582.

62. Ma YJ, Chen Y, Li L, et al. Trabecular bone imaging using a 3D adiabatic inversion recovery prepared ultrashort TE cones sequence at 3T. *Magn Reson Med*. 2020;83:1640-1651.

63. Breighner RE, Endo Y, Konin GP, Gulotta LV, Koff MF, Potter HG. Technical developments: Zero echo time imaging of the shoulder: Enhanced osseous detail by using MR imaging. *Radiology*. 2018;286:960-966.

64. Wiesinger F, Sacolick LI, Menini A, et al. Zero TE MR bone imaging in the head. *Magn Reson Med*. 2016;75:107-114.

SUPPORTING INFORMATION

Additional Supporting Information may be found online in the Supporting Information section.

FIGURE S1 Upper row shows the simulated UTE images of a Shepp–Logan phantom (truth). The k-space data were generated using NUFFT encoding along the GIRF-corrected trajectories. Images were then reconstructed using the nominal-corrected gradients, nominal-corrected and delayed-gradients and the GIRF-corrected gradients. A negative delay corresponds to a negative shift in time of the readout gradient. The time between two sampling points was 2 µs. Bottom row shows differences between the input image (truth) and the correspondingly reconstructed images. Blurring was introduced in the UTE images reconstructed with the nominal-corrected trajectory. At the object-background border, the nominal reconstructed image had more energy in the background region (arrow A) and showed an overshoot of signal intensity at object borders between regions with high and low signals (arrow B). Delaying the readout gradient, positive or negative, did not improve the image quality

FIGURE S2 Measurement of a spherical water phantom with the imaging plane being in three different geometrical orientations: coronal, sagittal and transversal. Here the z-axis points in feet-head direction, the y-axis points in anterior-posterior and the x-axis points in right-left direction. The line profiles on the right correspond the signal intensity along the arrows on the left

FIGURE S3 Data processing steps of the GMTF estimation. A) Uncorrected phase evolution in time of the signal originating from off-center slices. The phase follows the applied chirp test gradient waveform (green) that was applied once in positive and once in negative readout direction. The measured phase in opposing readout direction yields the background corrected phase (right). Here the background corrected phase for four different off-center locations is shown in time. B) Background corrected phase at different points in time along the measured slice locations. C) Measured phase at one time point at four different off-center locations and the secod order fit (left) and the corresponding root mean squared error (right). D) Root mean squared error of the second order fit for the four different locations and its evolution in time. The RMSE increases with increasing frequency of the chirp. For the highest frequencies and the highest RMSE the error is maximal ~0.06%

FIGURE S4 Comparison of two independent GIRF measurements with a time separation of one month. A) and B) magnitude and phase of the first order GIRF. C) and D) difference in magnitude and phase of the two measured first order GIRFs